FULL PAPER

Use of Fourier phase characteristics and effective stress analyses for post-earthquake ground motion estimation: application to ESG6 blind prediction steps 2&3 dataset and JMA accelerometric data

Atsushi Nozu[1*]

Abstract

After the occurrence of a large earthquake, engineering seismologists are often requested to estimate strong ground motions at a site where strong motion data were not obtained. The goal of this study was to test the ability of a class of methods that uses Fourier phase characteristics for the post-earthquake ground motion estimation, making use of the precious opportunity provide by the ESG6 Blind Prediction Steps 2&3. It was also part of the goal of this study to test the performance of the effective stress analyses to account for soil nonlinearity. In addition to the dataset provided by the organizer of the blind prediction, the author used additional accelerometric data from a nearby JMA site. To simulate ground motions for an M5.9 earthquake at the target site "KUMA", the Fourier amplitude spectrum was estimated from the spectral ratio between KUMA and the nearby JMA site. The Fourier phase spectrum was approximated by the spectrum of another event at KUMA. Comparison between the estimated and recorded ground motions after the blind prediction revealed that the estimated ground motions were fairly consistent with the observed ground motions, indicating the effectiveness of the method when the rupture process of the target event is simple and the soil nonlinearity at the target site is not significant. To simulate ground motions at KUMA for the M6.5 foreshock and the M7.3 mainshock of the 2016 Kumamoto earthquake sequence, the author conducted effective stress analyses using a program called "FLIP" to account for soil nonlinearity. Comparison between the estimated and recorded ground motions after the blind prediction indicated that the low-frequency components were overestimated and the high-frequency components were underestimated. The strong soil nonlinearity considered in the effective stress analyses was the main cause of the discrepancy. One explanation for this result could be that the nonlinear soil behavior at KUMA during the foreshock and the mainshock was not a strong one. Another explanation could be that the effect of soil nonlinearity was already included in the records at JMA and the effect of soil nonlinearity was double counted in the results submitted by the author.

Keywords Site effect, Fourier phase spectrum, Soil nonlinearity, Effective stress analysis, FLIP
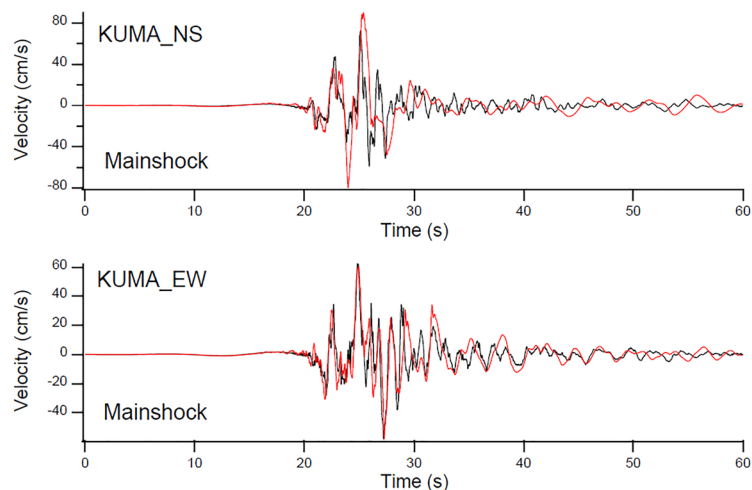
---

*Correspondence:
Atsushi Nozu
nozu@p.mpat.go.jp
Full list of author information is available at the end of the article

Graphical Abstract

Velocity waveforms at KUMA estimated with effective stress analyses and submitted for the blind prediction Step 3 for the mainshock (red traces) are compared with the observed velocity waveforms (black traces). In addition to the dataset provided by the organizer of the blind prediction, the author used additional accelerometric data from a nearby JMA site. The low frequency components tended to be overestimated especially for the NS component.

Introduction

After the occurrence of a large earthquake, engineering seismologists are often requested to estimate strong ground motions at a site where strong motion data were not obtained. The estimated ground motions are typically used for the response analysis of structures for the purpose of revealing the damage mechanism of a structure, restoring a damaged structure, or validating the design method itself. In line with recent advances in the design method, not only ground motion indices such as peak ground acceleration, peak ground velocity and response spectral values but also time histories of ground motions are required (e.g., International Organization for Standardization 2005).

Methods used for the post-earthquake estimation of ground motions broadly fall into two categories. One of them involves ground motion simulations based on a fault model of the target earthquake (e.g., Hutchings and Jarpe 1996; Kamae and Irikura 1998). This is similar to ground motion simulations for a scenario earthquake, but can be based on a fault model constrained by strong motion data of the target event. Therefore, uncertainty could be reduced compared to ground motion simulations for a hypothetical scenario earthquake. However, uncertainties are still involved in the fault model and the Green's functions. The other category of the methods for the post-earthquake ground motion estimation relies

on a ground motion record obtained at a nearby strong motion station and modifies it to account for the difference of the site-effect between the target site and the strong motion station (e.g., Hata et al. 2011). The modification can be based on either numerical or empirical methods. In this category of the methods, the reliability of the result is high if the strong motion station is very close to the target site, which is not always the case. It should be noted that, irrespective of the choice of the method, post-earthquake estimation of ground motions cannot necessarily be performed under ideal circumstances. One single method may not always be the best method; the best method may be dependent on the available information. Therefore, it is necessary to be flexible on the choice of the method.

One of the data that can contribute to improving the reliability of the post-earthquake ground motion estimation is the weak motion data collected at the target site. Therefore, aftershock observations are often conducted at a damaged area after a damaging earthquake (e.g., Yamanaka et al. 2016). The existence of weak motion data at the target site makes it possible to empirically evaluate the difference of the site effects between the target site and a nearby strong motion station. In particular, the Fourier spectral ratio between the two sites is often used to correct the Fourier amplitude spectrum observed at a strong motion station for the target event to estimate

the Fourier amplitude spectrum at the target site for the same event (e.g., Hata et al. 2011; Danmura et al. 2013). In these methods, to complete the estimation process of the time history of ground motions, we need additional information regarding the Fourier phase.

The derivative of the Fourier phase with respect to angular frequency is referred to as a group delay and related to the temporal characteristics of a ground motion (e.g., Sawada et al. 1998; Beauval et al. 2003; Boore 2003). It has been pointed out that the group delay is the sum of the source, path and site effects (e.g., Sawada et al. 1998; Beauval et al. 2003). Some authors proposed empirical relations to estimate the mean and the standard deviation of group delays in different frequency bands based on magnitude and distance (e.g., Satoh et al. 1997; Sato et al. 2000). These relations are intended to be used based on the assumption that the group delays for different frequencies are independent to each other (e.g., Satoh et al. 1997; Sato et al. 2000). However, there is a limitation in the reality of a simulated Fourier phase based on this assumption because it can be theoretically shown that the Fourier phase spectrum of an earthquake motion is differentiable and the group delay is a continuous function of frequency except for a frequency for which the Fourier amplitude is zero (Nozu 2017, 2022), which indicates that the group delay times for neighboring frequencies are not independent.

In recognition of this limitation, another class of methods has been proposed in which the Fourier phase of a single event is used. For example, Hata et al. (2011) proposed to use the Fourier phase characteristics of a weak motion record obtained at the target site. Danmura et al. (2013) used the Fourier phase characteristics for the target event at the strong motion station. In any case, it is an important issue to test the accuracy of the methods for different events.

The organizers of ESG6 planed a blind prediction regarding strong motion simulations (Matsushima et al. 2022; Chimoto et al. 2022; Tsuno et al. 2022). The goal of Steps 2&3 of the blind prediction was to estimate weak and strong ground motions, respectively, at a target site located in the near-source region of the 2016 Kumamoto, Japan, earthquake sequence. The records at the target site for the target events were concealed from the participants, but some weak motion records at the target site were provided by the organizer. Therefore, it was possible to evaluate the difference of the site amplification factor between the target site and a nearby strong motion station empirically. The goal of this study was to make use of this precious opportunity and to test the ability of the class of methods that uses Fourier phase characteristics.

Another issue that affects the accuracy of the post-earthquake estimation of ground motions is soil nonlinearity (e.g., Aki 1993; Beresnev and Wen 1996). The goal of Step 3 of the blind prediction was to estimate ground motions during the M6.5 foreshock and the M7.3 mainshock of the Kumamoto earthquake sequence. For these earthquakes, the organizer of the blind prediction suggested us to pay attention to the effects of soil non-linearity. To account for soil nonlinearity, the author conducted effective stress analyses using a program called "FLIP" (Iai 1991; Iai et al. 1992). It was also part of the goal of this study to test the performance of the effective stress analyses.

This article describes the methods employed by the author and the results for the ESG6 Blind Prediction (Matsushima et al. 2022; Chimoto et al. 2022; Tsuno et al. 2022) Steps 2&3. In the following, first, the methods employed by the author are described. Then, the ensuing sections describe how the methods were applied to Steps 2&3, respectively. After the blind prediction, the records at KUMA for the target events were distributed by the organizer. This article also shows the comparison between the estimated and recorded ground motions and discusses some lessons learned from the blind prediction. It should be noted that, in addition to the dataset provided by the organizer of the Blind Prediction, the author used additional accelerometric data from a nearby JMA site. The results of this article benefitted from using the additional data.

Method

Figure 1 shows the methods employed by the author. In this figure, the reference site corresponds to a strong motion station where the target earthquake was observed and does not correspond to a site with a site amplification factor of unity. First the Fourier transform is applied to the time history of the observed ground motion to obtain the Fourier amplitude at the reference site. Then the Fourier amplitude at the reference site is multiplied by the empirical spectral ratio between the target site and the reference site to obtain the Fourier amplitude at the target site. The empirical spectral ratio is obtained based on weak motion records obtained for common events at the target site and the reference site. Examples will be shown in the ensuing sections.

There are two ways of determining the Fourier phase characteristics at the target site. In the site-effect substitution method proposed by Hata et al. (2011), the Fourier phase spectrum at the target site for a selected event is used. This method is effective if the selected event and the target event share the same path and site effects and the source effect is not a dominant factor for the Fourier phase spectra. These conditions apply to Step 2 as shown later. However, if the rupture process of the target event is complex, the applicability of the method is restricted. For
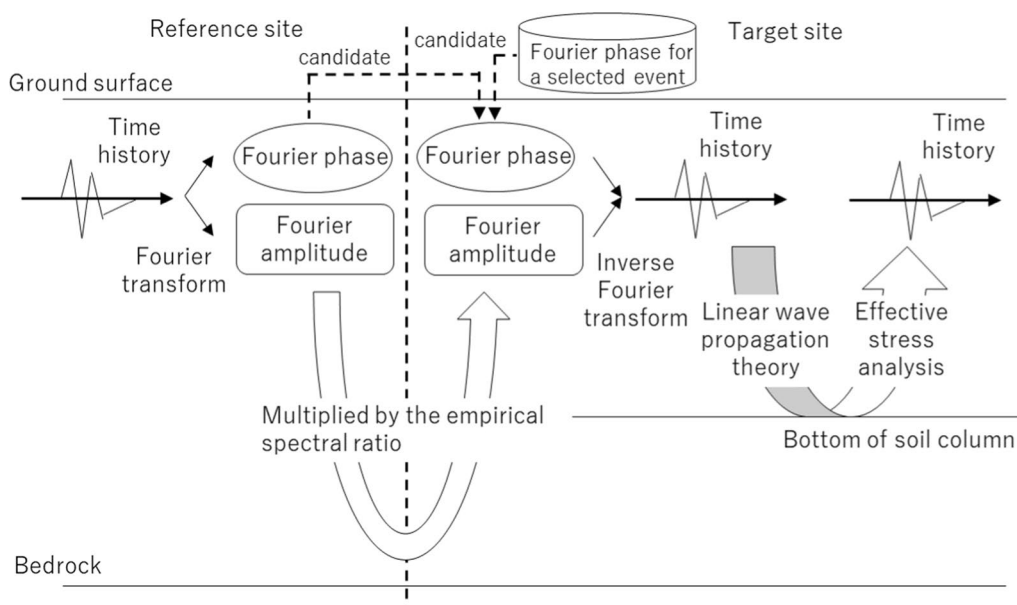
Fig. 1 Methods employed by the author. The Fourier amplitude at the target site is estimated based on the empirical spectral ratio. Once the Fourier amplitude and phase at the target site are determined, the inverse Fourier transform is applied to generate the time history of ground motions at the target site. To account for soil nonlinearity, effective stress analyses are conducted

example, if the rupture of more than one asperity affects the ground motion for the target event, the Fourier phase spectrum will also be affected by the arrival of multiple pulses and cannot be represented by the Fourier phase spectrum of another event. For such cases, an alternative way of determining the Fourier phase characteristics at the target site is to simply use the Fourier phase characteristics at the reference site for the target event (Danmura 2013). The applicability of these methods for Steps 2&3 will be investigated in the ensuing sections.

Once the Fourier amplitude and phase at the target site are determined, the inverse Fourier transform can be applied to generate the time history of ground motions at the target site. The estimated ground motions can be written in the frequency domain as follows:

$$F(\omega) = A(\omega)O(\omega)/|O(\omega)|_p, \tag{1}$$

where $F(\omega)$ is the Fourier transform of the estimated ground motion at the target site (complex value), $A(\omega)$ is the Fourier amplitude at the target site (real value), $O(\omega)$ is the Fourier transform of the selected record to determine the Fourier phase (complex value) and $|O(\omega)|_p$ is its amplitude, smoothed with a Parzen window of 0.05 Hz (real value). In this expression, a Parzen window is used to intentionally keep small ripples in $O(\omega)$, which is essential for generating a causal time history (Nozu et al. 2009). One of the main features of the present method is that the Fourier phase characteristics of a single event is used rather than averaging Fourier phase spectra of

different events. Averaging was avoided because it often affects the causality of generated time histories. The appropriateness of using the Fourier phase characteristics of a single event was shown by Hata et al. (2011) and will be tested in the later sections of this article.

Finally, the following procedure is applied to account for the nonlinear soil behavior:

(1) Deconvolve the linear soil response to estimate outcrop motions for a sufficiently stiff base layer based on linear one-dimensional wave propagation theory (Kanai 1952; Lysmer et al. 1971). The base outcrop motions are sometimes referred to as "2E motions", because Schnabel et al. (1972) abbreviated the incident and reflected waves as "E" and "F", respectively, and the base outcrop motions are twice the incident wave.

(2) Estimate surface ground motions with effective stress analyses. In this study, the author uses a program called "FLIP" (Iai 1991; Iai et al. 1992). This program can consider positive and negative dilatancy and the generation of excess pore water pressure for sandy soils. Since its successful application to damage case histories of port structures during the 1995 Kobe earthquake (Iai et al. 1998), it has been extensively used in the design of port structures in Japan. Its application to one-dimensional soil columns were documented by Iai et al. (1995), Tobita et al. (2010) and others. This program is

equipped with the viscous boundary devised by Lysmer and Kuhlemeyer (1969), which enables to apply ground motions with considerations of the elasticity of the base layer. Therefore, the base outcrop motions obtained in (1) can be applied.
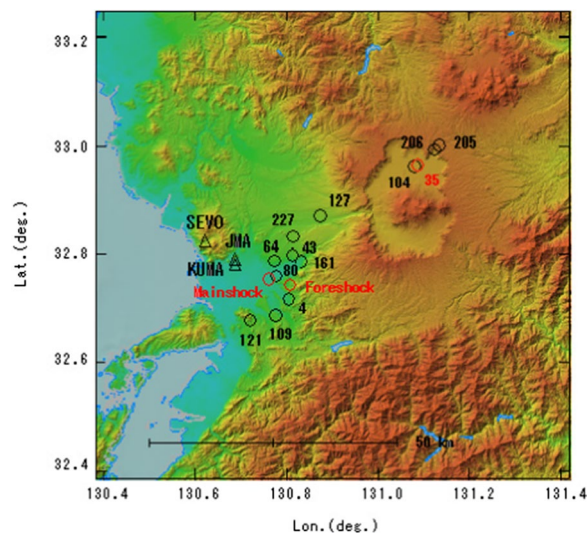

Fig. 2 Epicenters of the earthquakes and the locations of the observation stations. The triangles labeled as KUMA, SEVO and JMA are the observation stations. Among them, KUMA is the target site. The circles indicate the epicenters of the earthquakes. The numbers correspond to those in Table 1. The red circles indicate the target earthquakes of the blind prediction. No.35 is the M5.9 target event for Step 2. The M6.5 foreshock and the M7.3 mainshock are the target events for Step 3. The black circles show the earthquakes for which ground motion data at KUMA were provided by the organizer for the blind prediction

The ensuing sections are devoted to describe how these methods were applied to Steps 2&3, respectively.

Step 2—simulation of weak motions

The goal of Step 2 was to estimate ground motions at a target site called "KUMA", located at 32.7756N, 130.6879E, shown in Fig. 2, during the M5.9 target event that occurred in April 16, 2016, 3:03 (JST), approximately 1.5 h after the mainshock of the 2016 Kumamoto earthquake sequence. In this article, all the magnitude are those determined by the Japan Meteorological Agency (JMA). The target event (No.35 in Table 1 and Fig. 2) occurred in the Aso region.

Reference site

Ground motion data at KUMA were provided by the organizer for all the events listed in Table 1 except for the event No.35, which was the target event. The organizer also provided ground motion data at a station called "SEVO", shown in Fig. 2. However, the author decided to use another station operated by JMA (32.7866N, 130.6876E) as a reference station (the station will be abbreviated as JMA), because the station is closer to KUMA as shown in Fig. 2. In fact, it is only 1.2 km north of KUMA. Table 1 shows the availability of records at JMA.

Fourier amplitude spectrum

Figure 3 shows the Fourier amplitude spectra observed at KUMA and JMA for five events with $M \geq 4.5$ (No.64, No.104, No.109, No.205, No.206) for the horizontal components. The Fourier spectra are in terms of the

Table 1 Parameters of the earthquakes. The parameters are shown for the earthquakes for which ground motion data at KUMA were provided by the organizer and the M5.9 target event for Step 2

No.	Y	M	D	H	M	S	Lat	Lon	Depth(km)	MJ	KUMA	JMA
4	2016	4	16	1	5	42.48	32.71633	130.80483	15.46	3.3	o	x
35	**2016**	**4**	**16**	**3**	**3**	**10.78**	**32.96383**	**131.08683**	**6.89**	**5.9**	**x**	**o**
43	2016	4	16	4	5	49.2	32.79733	130.81317	12.29	4.0	o	o
64	2016	4	16	7	23	54.32	32.78667	130.77383	11.93	4.8	o	o
80	2016	4	16	11	2	51.71	32.75833	130.77817	14.57	4.4	o	o
104	**2016**	**4**	**17**	**0**	**14**	**51.69**	**32.96167**	**131.07917**	**8.92**	**4.8**	**o**	**o**
109	2016	4	17	4	46	49.09	32.68717	130.77617	10.32	4.5	o	o
121	2016	4	17	19	23	41.22	32.6775	130.72067	10.58	4.4	o	o
127	2016	4	18	8	35	43.02	32.8695	130.87333	10.2	4.2	o	o
161	2016	4	21	21	52	3.39	32.78533	130.83183	10.98	4.0	o	o
205	**2016**	**5**	**5**	**10**	**31**	**30.47**	**33.00033**	**131.13417**	**11.16**	**4.6**	**o**	**o**
206	**2016**	**5**	**5**	**10**	**40**	**12.83**	**32.99283**	**131.12217**	**10.81**	**4.9**	**o**	**o**
227	2016	5	19	2	37	44.28	32.83133	130.81417	16.43	3.9	o	x

The numbers correspond to those in Fig. 1. No.35 is the target event for Step 2. Earthquakes that occurred in the Aso region are highlighted by bold fonts

o the records were available. *x* the records were not available during the blind prediction
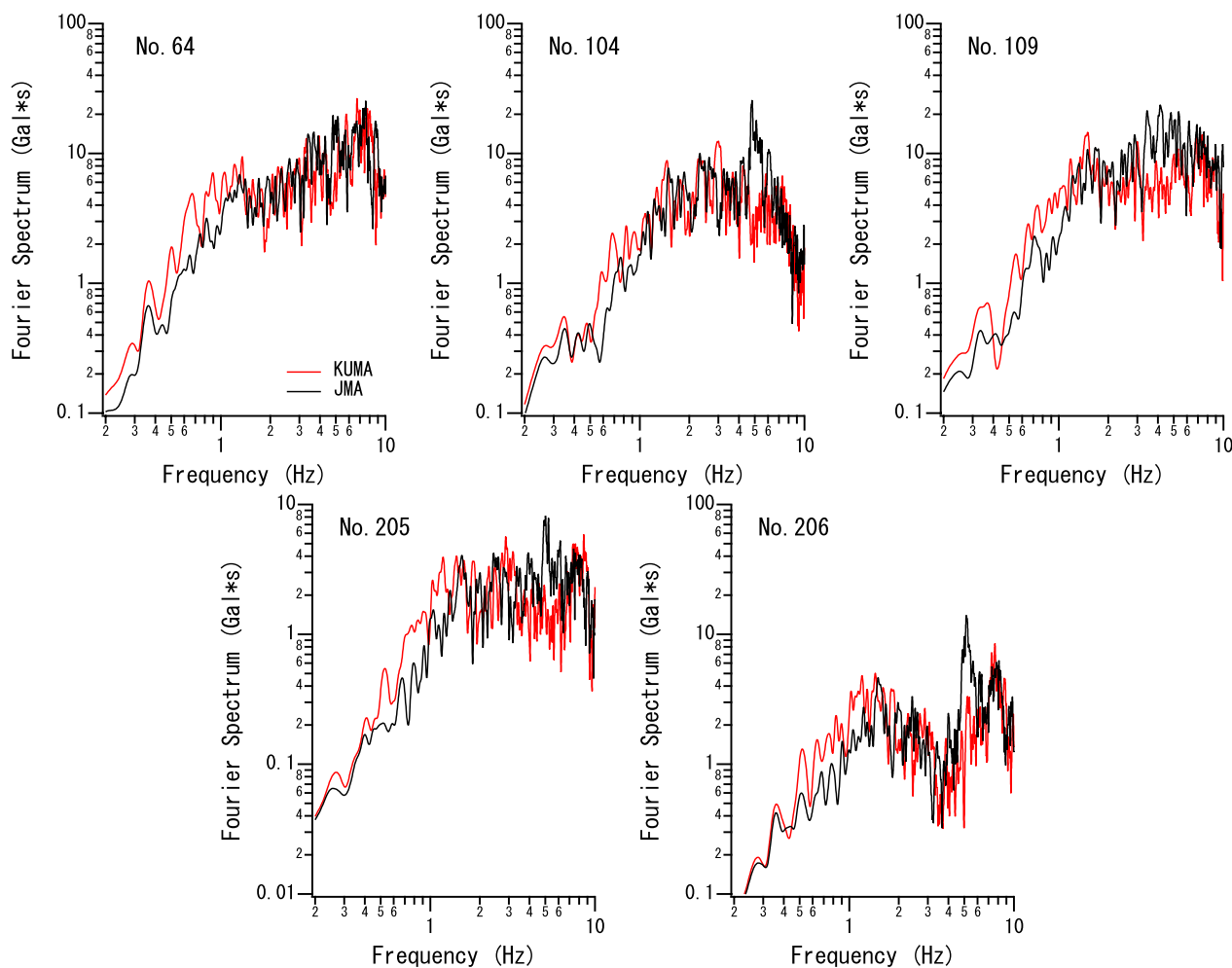
Fig. 3 Fourier amplitude spectra observed at KUMA and JMA. The Fourier spectra are shown for the five events with M ≥ 4.5 (No.64, No.104, No.109, No.205, No.206) for the horizontal components. The Fourier spectra are in terms of the vector sum of two horizontal components, smoothed with a Parzen window of 0.05 Hz

vector sum of two horizontal components, smoothed with a Parzen window of 0.05 Hz. The Fourier spectra are shown for events with $M \geq 4.5$ because the records in this range of magnitude typically exhibit good S/N ratio down to 0.2 Hz. In Fig. 3, we find a robust tendency for the frequency components of 0.5–1.2 Hz to be greater for KUMA than for JMA. The top left panel of Fig. 4 shows the Fourier spectral ratios between KUMA and JMA for the five events. The spectral ratios are greater than one for the frequency components of 0.5–1.2 Hz. The top right panel of Fig. 4 shows the geometric mean of the Fourier spectral ratios. In general, Fourier spectral ratios between different stations can depend on the location of the source. From such a point of view, it should be noted that the target event No.35 occurred in the Aso region (Fig. 2). On the other hand, the five events can be categorized into two groups: No.104, No.205 and No.206 occurred in the Aso region; No.64 and No.109 occurred

closer to the target site (Fig. 2). Therefore, the averaged ratio for the five events was compared with the averaged ratio for the three events that occurred in the Aso region in the top right panel of Fig. 4. As a result, the averaged ratio for the five events was not significantly different from that for the three events. This result indicated that the spectral ratios were not significantly affected by the source and path effects of the individual events. Therefore, the author decided to use the averaged ratio for the five events.

It should be noted that the target event No.35 occurred approximately 1.5 h after the mainshock. The organizer of the blind prediction suggested us to pay attention to the effects of soil nonlinearity for the mainshock at KUMA. Therefore, the effects of soil nonlinearity such as the remaining effects of excess pore water pressure might also be anticipated for the target event at KUMA. Furthermore, the S-wave amplitude was relatively small
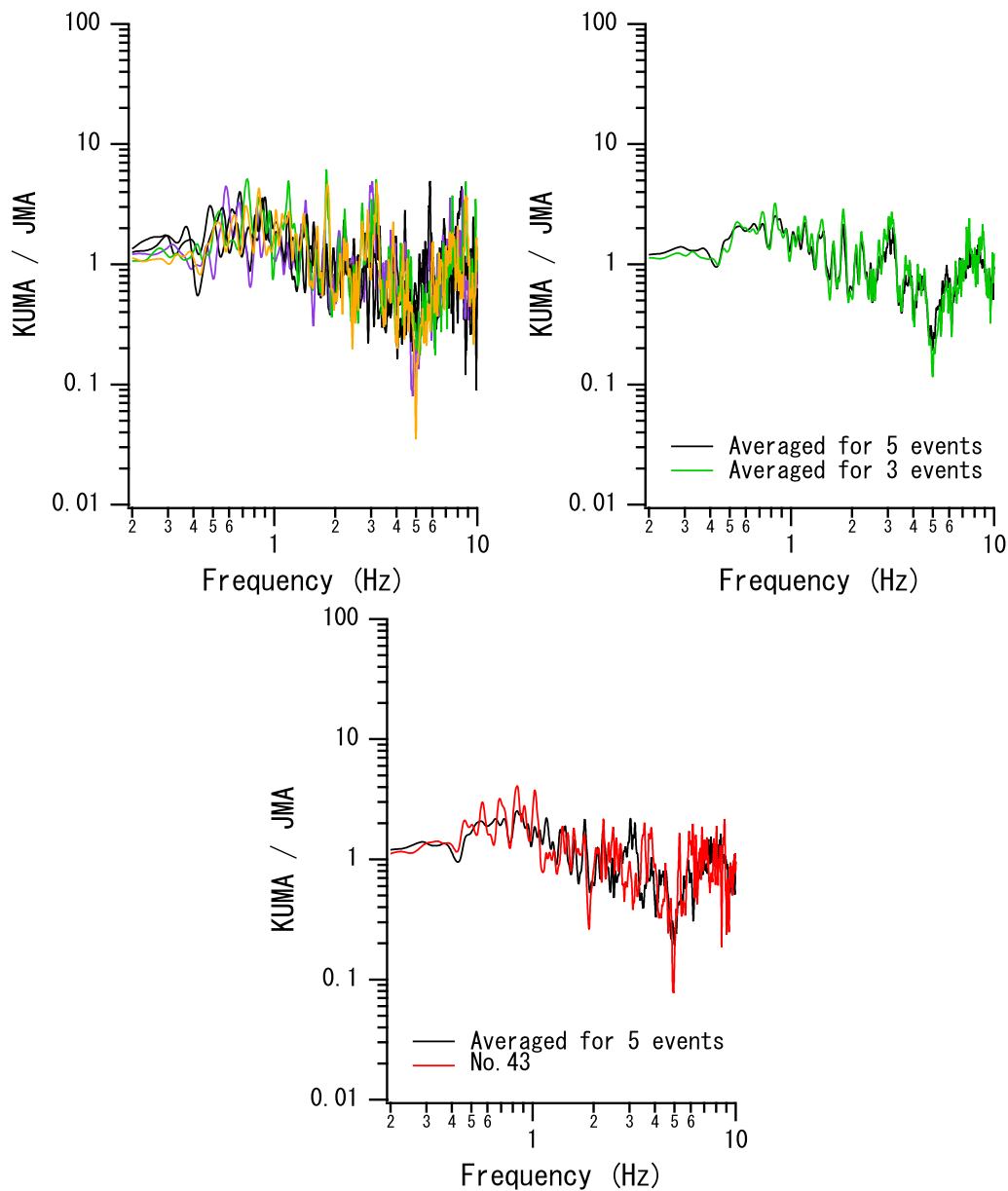
Fig. 4 Fourier spectral ratios between KUMA and JMA for the horizontal components. The top left panel shows the Fourier spectral ratios for the five events with M ≥ 4.5 (No.64, No.104, No.109, No.205, No.206) for the horizontal components. The top right panel shows their geometric mean. The geometric mean for the five events shown in the top left panel was compared with the geometric mean for the three events that occurred in the Aso region. The former was used for the ensuing simulation. The bottom panel compares the geometric mean for the five events with the spectral ratio for the event No.43, which occurred approximately 2.5 h after the mainshock

compared to the P-wave amplitude for the event No.43, which was the earliest available event after the mainshock at KUMA (Table 1), which could also be indicative of soil nonlinearity. For this reason, the author compared the spectral ratio for the event No.43 with the averaged spectral ratio in the bottom panel of Fig. 4. As a result, the author could not find any evidence of soil nonlinearity such as the shift of the peak frequency to lower frequencies or the amplitude decrease for higher frequencies for the event No.43, which occurred approximately 2.5 h after the mainshock (Table 1). Therefore, the author assumed that there was no strong nonlinear effect at KUMA during the target event that occurred approximately 1.5 h after the mainshock.

The spectral ratio for the vertical component was evaluated in a similar way. The results are shown in

Additional file 1: Figure A1 [see appendix.pdf]. Again, the averaged ratio for the five events was not significantly different from that for the three events. Therefore, the author decided to use the averaged ratio for the five events.

Fourier phase spectrum

In general, Fourier phase characteristics of a ground motion significantly depend on the location of the source. It is obvious from Fig. 2 that, among available events, the event No.104 was closest to the target event No.35. Therefore, the author decided to approximate the Fourier phase spectrum at KUMA for the target event with the Fourier phase spectrum at the same station for the event No.104.

To confirm the appropriateness of this decision, the author investigated the similarity of the Fourier phase characteristics between the target event and the event No.104 at JMA. Let us assume that we have a common Fourier amplitude spectrum and two different Fourier phase spectra. Then, each of the Fourier phase spectrum can be "mapped" into a time history. In general, it is a difficult task to measure the difference of two different Fourier phase spectra in the frequency domain, because it is difficult to understand how a small perturbation in a Fourier phase spectrum will affect the resultant time history. Therefore, in this article, we propose to measure the difference of Fourier phase spectra not in the original space but in the mapped space; two different Fourier phase spectra are defined similar if the resultant time histories are similar. This definition is rational because, after all, we are interested in the similarity of the time histories. When the author joined the blind prediction experiment, the similarity of the time histories was evaluated by visual inspection. In the future, it is preferable to establish a quantitative measure to select an appropriate event. Figure 5 compares the observed velocity waveforms for the target event at JMA and the phase-exchanged velocity waveforms in which the Fourier amplitude of the target event and the Fourier phase of the event No.104 were combined. The waveforms (black and red) share the same Fourier amplitude, but have different Fourier phase characteristics. Figure 5 indicates that the waveforms are similar, indicating the similarity of the Fourier phase characteristics between the target event and the event No.104 at JMA. The result supported the decision to use the Fourier phase spectrum of the event No.104 at KUMA in the site-effect substitution method.

Results

The author applied the site-effect substitution method. The horizontal components were estimated based on the horizontal spectral ratio shown in Fig. 4. The vertical component was estimated based on the vertical spectral ratio shown in Additional file 1: Figure A1 [see appendix. pdf].

In Fig. 6, the acceleration waveforms estimated and submitted by the author for the blind prediction Step 2 are compared with the recorded acceleration waveforms, which were distributed by the organizer after the blind prediction. The origin of the horizontal axis corresponds to April 16, 2016, 3:03:10 (JST). It can be pointed out that there is an error in the arrival time of the main energy. When the author submitted the results, the author did not make any rigorous investigation in terms of the origin of the time history. After the recorded waveforms were distributed, the author found that, although the events No.35 and No.104 occurred at similar locations (Fig. 2 and Table 1), the arrival of the S waves were delayed for the event No.35 compared to the event No.104 both for KUMA and JMA. The author cannot find any good explanation for this tendency. Therefore, in this article, the author decided to simply shift the estimated waveforms so that the arrival time of the S-wave be consistent between the estimated and recorded waveforms. Figure 7 compares the estimated acceleration waveforms after the time shift with the recorded acceleration waveforms. Figure 8 compares the estimated velocity waveforms after the time shift with the velocity waveforms calculated from the records. Figure 9 compares the estimated Fourier spectra with the Fourier spectra calculated from the records. These comparisons reveal that, except for the error in the arrival time, the estimated ground motions were fairly consistent with the observed ground motions. Especially the velocity waveforms were reproduced well including the later phases. The goodness of fit was evaluated based on Anderson's (2004) criteria. Throughout this article, the author used the S2 score, which can be obtained by averaging the scores on ten different criteria. The result was 7.8, 7.8 and 8.3 for the NS, EW and UD broadband waveforms, respectively. The result indicates the effectiveness of the site-effect substitution method in estimating ground motions after an earthquake at a site where the ground motions are unknown as long as aftershock records are available at the site.

Step 3—simulation of strong motions

The goal of Step 3 was to estimate ground motions at KUMA during the M6.5 foreshock and the M7.3 mainshock of the Kumamoto earthquake sequence. For this step, the organizer of the blind prediction suggested us to pay attention to the effects of soil nonlinearity. Therefore,
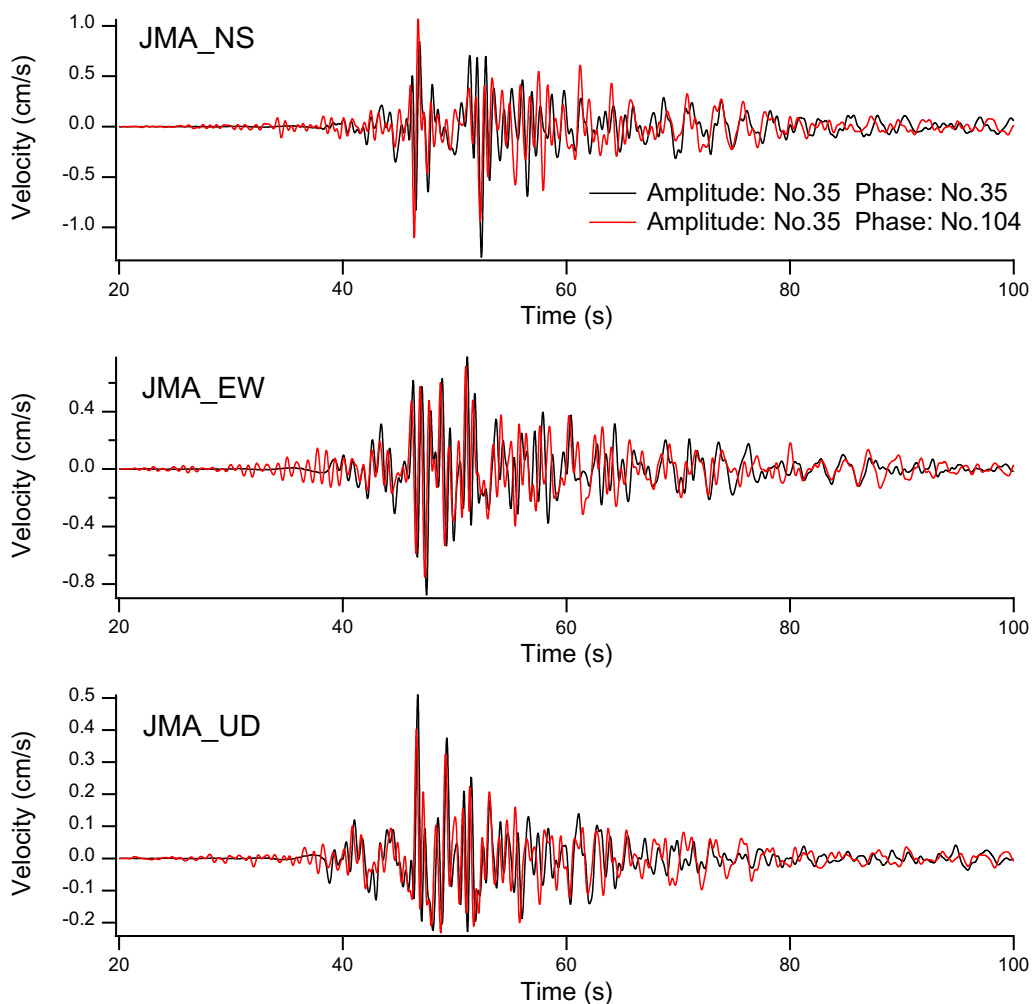
Fig. 5 Similarity of the Fourier phase characteristics between the events No.35 and No.104 at JMA. The observed velocity waveforms for the target event No.35 at JMA (black traces) and the phase-exchanged velocity waveforms in which the Fourier amplitude of the target event and the Fourier phase of the event No.104 are combined (red traces). Both traces are in the frequency range of 0.2–2 Hz

to account for soil nonlinearity, the author conducted effective stress analyses following the procedure shown in Fig. 1. In this procedure, it is necessary to choose a sufficiently stiff base layer. In this application, the author chose a gravel layer that exists at a depth of 31 m (ground level—31 m; GL—31 m) as the base layer. This procedure implies that the effect of soil nonlinearity at the reference site JMA, if any, is neglected. This fact will be discussed later.

Applicability of the site-effect substitution method

One of the main features of the site-effect substitution method is that the Fourier phase spectrum at the target site for the target event is approximated by the Fourier phase spectrum at the same site for another event. This operation is effective if the two events share the same path and site effects and the source effect is not a dominant factor for the Fourier phase spectra. These conditions applied to Step 2. However, it was anticipated that the latter condition does not apply to Step 3 due to the complexity of the rupture process especially for the mainshock (Asano and Iwata 2016; Nozu and Nagasaka 2017). Therefore, the author investigated the similarity of the Fourier phase characteristics between the target events and other available events at JMA.

In Fig. 10, the similarity of the Fourier phase characteristics is examined between the mainshock and the event No.161 at JMA. Among available events, the event No.161 produced the best results for the mainshock. This is presumably because the event No.161 (Fig. 2) occurred near the asperities of the mainshock (Asano and Iwata 2016; Nozu and Nagasaka 2017) and this event conveyed similar path and site effects with the mainshock. However, the large-amplitude phase for the EW and UD
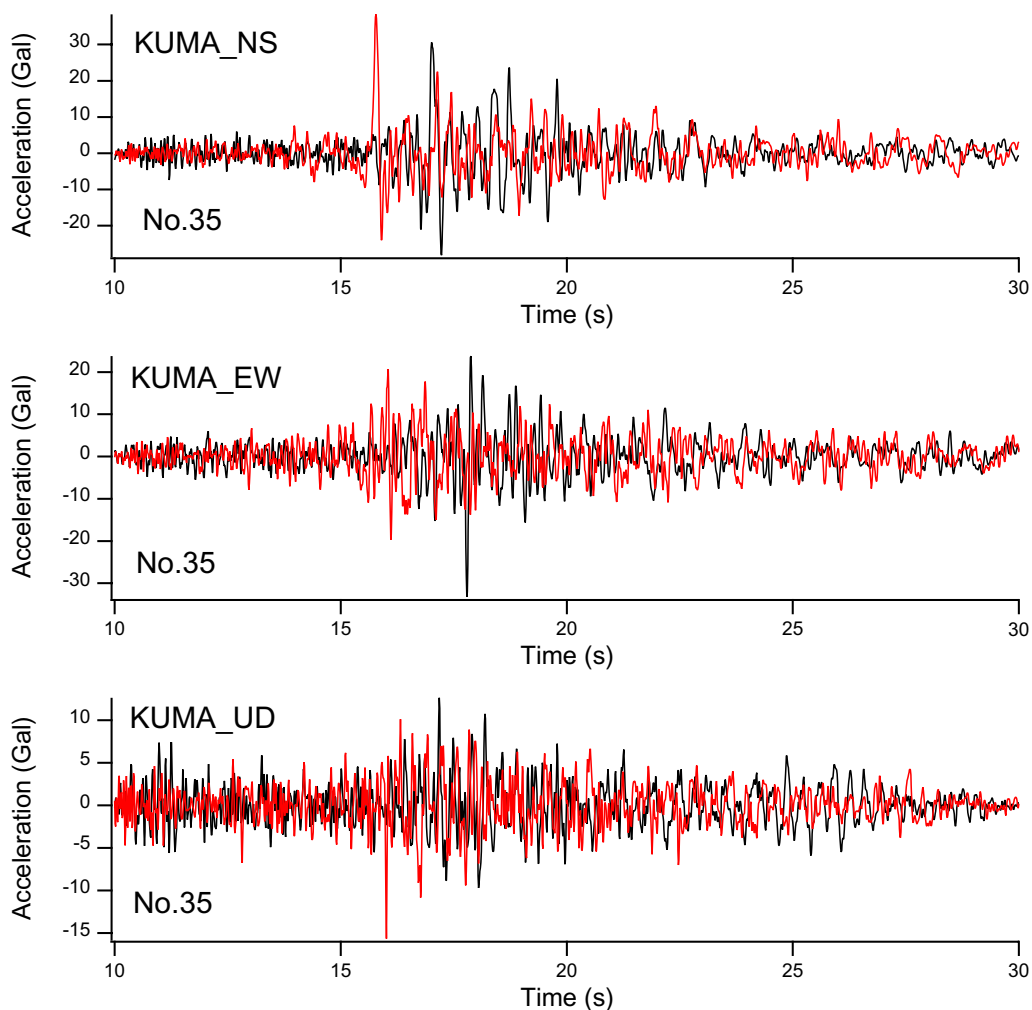
Fig. 6 Acceleration waveforms estimated and submitted for the blind prediction Step 2. The acceleration waveforms estimated and submitted by the author for the blind prediction Step 2 (red traces) are compared with the recorded acceleration waveforms (black traces), which were distributed after the blind prediction. The origin of the horizontal axis corresponds to April 16, 2016, 3:03:10 (JST). It can be pointed out that there is an error in the arrival time

components at approximately 27 s was not captured by the phase-exchanged waves. This is presumably because of the complexity of the rupture process of the mainshock. Therefore, the author avoided to use the site-effect substitution method for the mainshock.

The similarity of the Fourier phase characteristics was also examined between the foreshock and other available events at JMA. Among available events, the events No.64 and No.161 produced the best results for the foreshock as shown in Additional file 1: Figures A2 and A3 [see appendix.pdf], presumably because these events occurred near the asperities of the foreshock (Asano and Iwata 2016) and they conveyed similar path and site effects with the foreshock. The similarity of the waveforms indicated the potential applicability of the site-effect substitution

method to the foreshock. However, the author avoided using the site-effect substitution method for the foreshock simply because the author preferred using the same method for the foreshock and the mainshock.

Availability of the Fourier phase spectrum at JMA

Instead of using the site-effect substitution method, the author tested the similarity of Fourier phase characteristics between KUMA and JMA for several events.

Figure 11 shows the results for the event No.161. The Fourier phase characteristics at KUMA and JMA resemble each other at least for the horizontal components, although there is a notable difference for the vertical component. The author found that the degree of similarity depends on the event. However, the author
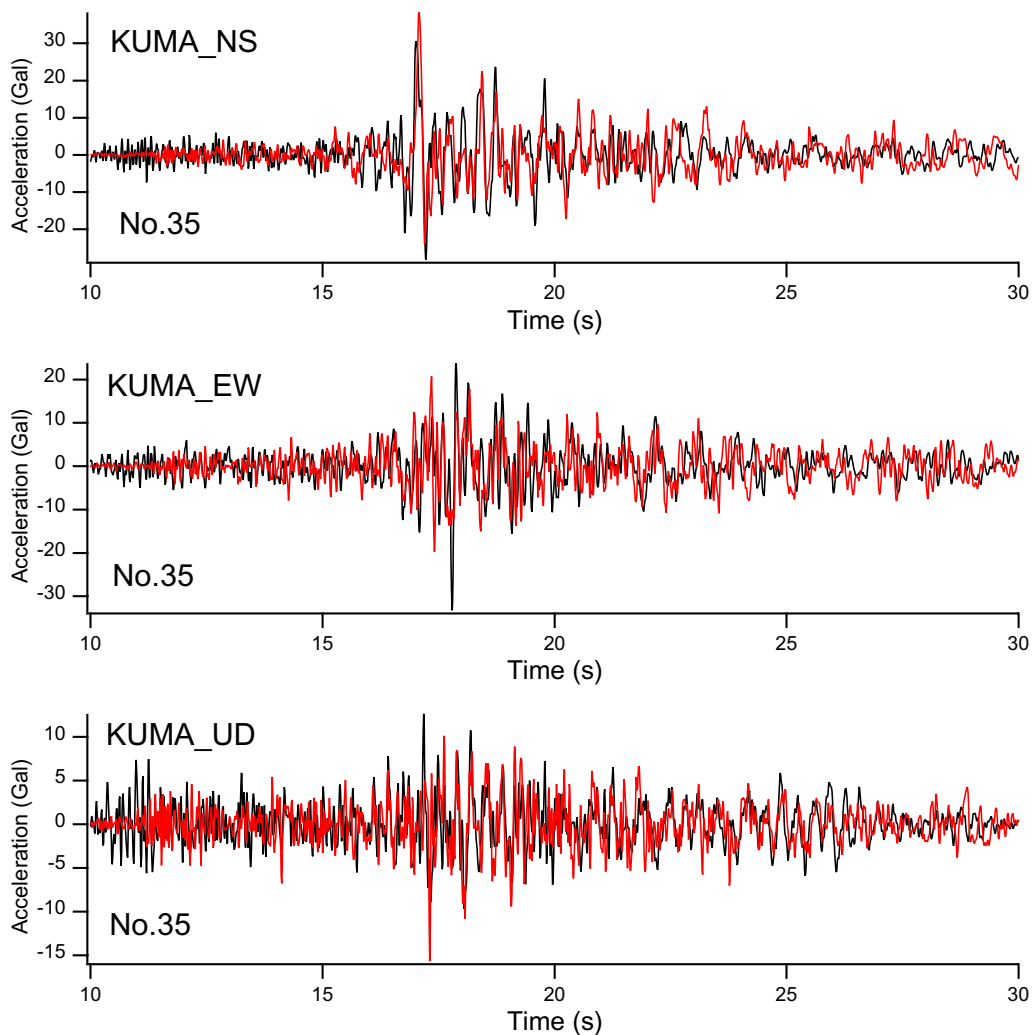
Fig. 7 Estimated acceleration waveforms for the blind prediction Step 2 after the time shift. The estimated acceleration waveforms for the blind prediction Step 2 after the time shift (red traces) are compared with the recorded acceleration waveforms (black traces), which were distributed after the blind prediction. The estimated waveforms were shifted so that the arrival time of the S-wave be consistent between the estimated and recorded waveforms

acknowledged the importance of the event No.161 because the event presumably conveys similar path and site effects with the foreshock and the mainshock. If the Fourier phase characteristics are similar for the event No.161 between KUMA and JMA, it could be reasonable to assume that they are similar also for the foreshock and the mainshock. Therefore, to estimate ground motions at KUMA during the foreshock and the mainshock under linear site response, the author simply used the Fourier phase characteristics at JMA for the same events.

Fourier amplitude spectrum

The Fourier amplitude spectra at KUMA during the foreshock and the mainshock were estimated in a similar way as in Step 2, that is, the Fourier amplitude spectra observed at JMA during the same events were multiplied by the spectral ratio shown in the top right panel of Fig. 4 for the horizontal components and the right panel of Additional file 1: Figure A1 [see appendix.pdf] for the vertical component. The author used the averaged ratios for the five events. To make sure that it is appropriate to use the averaged ratios for the five events, which did not necessarily occur near the target events, the author compared the averaged ratios for the five events with the spectral ratios for the event No.161, which presumably conveyed similar path and site effects with the target events as mentioned above. The results indicated that there is no significant difference between the spectral
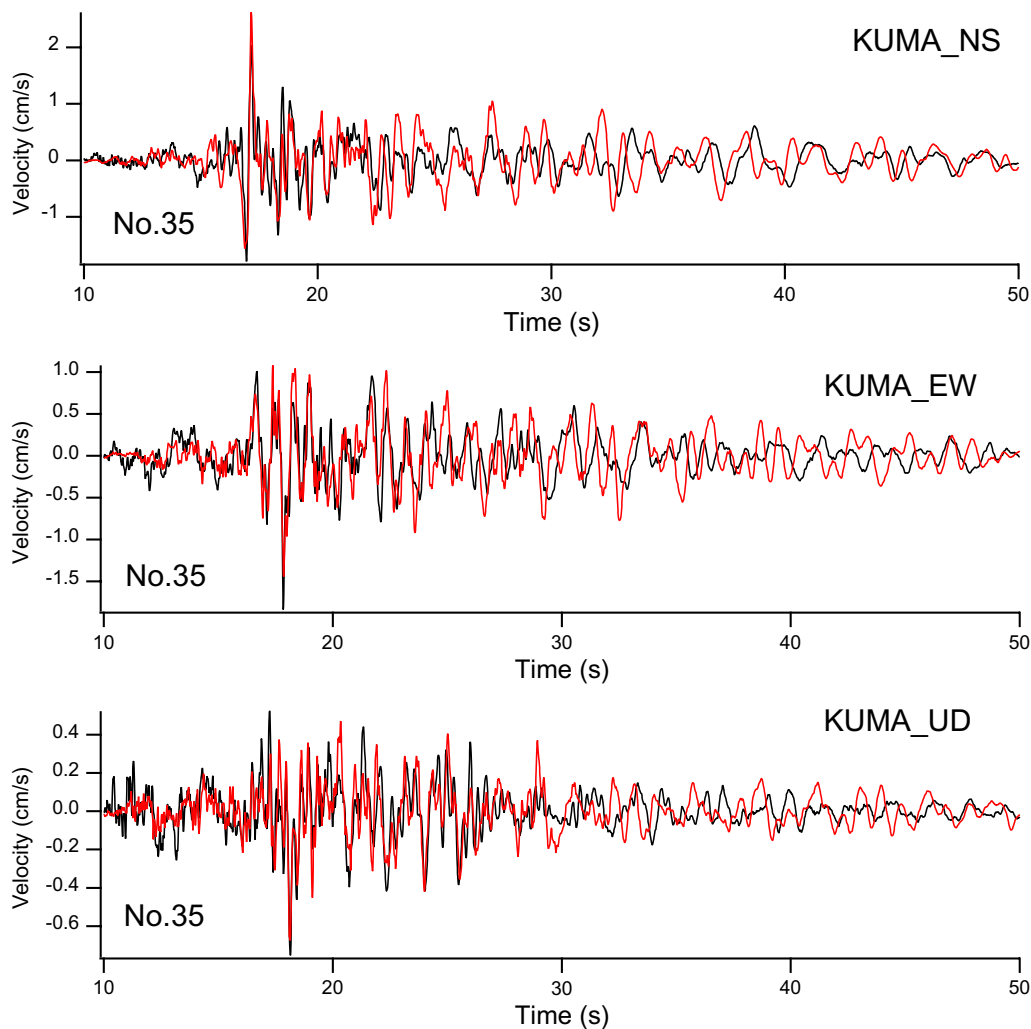
Fig. 8 Estimated velocity waveforms for the blind prediction Step 2 after the time shift. The estimated velocity waveforms for the blind prediction Step 2 after the time shift (red traces) are compared with the velocity waveforms calculated from the records (black traces). The estimated waveforms were shifted so that the arrival time of the S-wave be consistent between the estimated and recorded waveforms

ratios at least for the horizontal components. Therefore, the author used the averaged ratios for the five events.

Base outcrop motions based on linear one-dimensional wave propagation theory

Next, the base outcrop (2E) motions at GL—31 m were estimated based on linear one-dimensional wave propagation theory (Kanai 1952; Lysmer et al. 1971). The soil layers were divided as shown in Table 2 according to the PS logging results provided by the organizer of the blind prediction (Matsushima et al. 2022). For the horizontal components, the S-wave velocities were used. For the vertical components, the P-wave velocities were used. For the 2nd, 4th, 5th, 6th and 7th layers, laboratory test results were available. The corresponding samples were

T-1, T-2, Tr-3, Tr-4 and Tr-5, respectively. The author used the wet densities from the laboratory tests for these layers. For the 3rd, 8th and 9th layers, the author decided to use the same wet densities as the 6th, 6th and 5th layers, respectively, considering the similarity of the soils and N values. For the 1st layer and the base layer, the author assumed a density of 2.0 g/cm^3. The author used the damping coefficient of 0.02 for all the layers for all the analyses, referring to the results of cyclic triaxial tests.

Surface ground motions with effective stress analyses

Finally effective stress analyses were conducted to estimate surface ground motions under nonlinear site response. For this purpose, the author used a program called "FLIP" (Iai 1991; Iai et al. 1992). The parameters
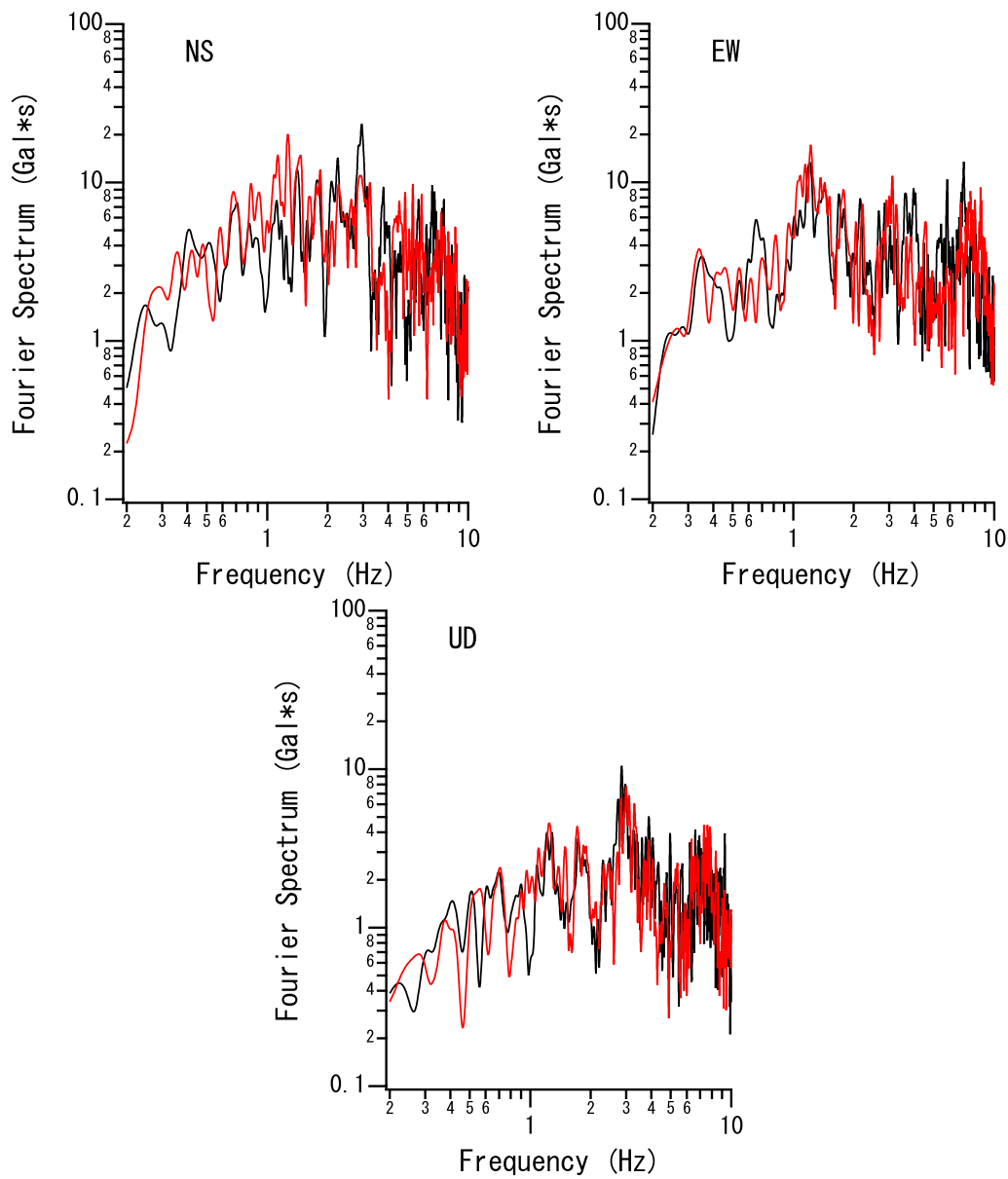
Fig. 9 Estimated Fourier spectra for the blind prediction Step 2. The estimated Fourier spectra for the blind prediction Step 2 (red traces) are compared with the Fourier spectra calculated from the records (black traces). The Fourier spectra are smoothed with a Parzen window of 0.05 Hz

were determined based on a simplified procedure (Morita et al. 1997) from the PS logging results, N values and fine particle content provided by the organizer (Matsushima et al. 2022).

Table 3 shows the parameters used for the effective stress analyses. In this program, the shear modulus G_m and the bulk modulus K_m for the soil skeleton at small strain depend on some power of the effective confining pressure σ'_m as follows:

$$G_m = G_{m0}\left(\sigma'_m/\sigma'_{m0}\right)^{m_G}, \tag{2}$$

$$K_m = K_{m0}\left(\sigma'_m/\sigma'_{m0}\right)^{m_K}. \tag{3}$$

They are specified for a reference effective confining pressure σ'_{m0}. In this analysis, the effective confining pressure at the center of each layer was selected as the
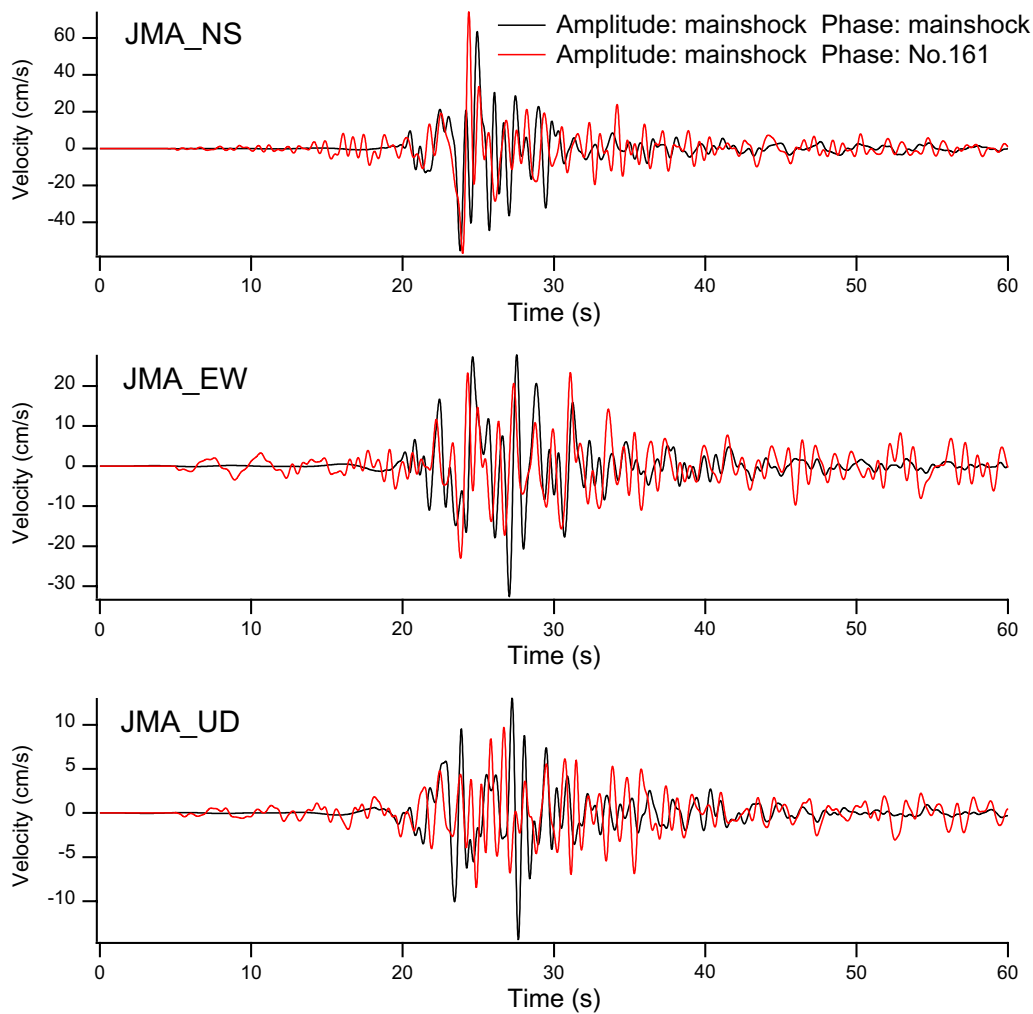
Fig. 10 Similarity of the Fourier phase characteristics between the mainshock and the event No.161 at JMA. The observed velocity waveforms for the mainshock at JMA (black traces) and the phase-exchanged velocity waveforms in which the Fourier amplitude of the mainshock and the Fourier phase of the event No.161 are combined (red traces). Both traces are in the frequency range of 0.2–2 Hz. The phase-exchanged wave for the NS component was multiplied by (− 1)

reference effective confining pressure. Then, the shear modulus at small strain G_{m0} for the reference effective confining pressure was determined from the PS logging results. The bulk modulus for the soil skeleton K_{m0} for the reference effective confining pressure was determined assuming a Poisson's ratio of 1/3. Then they were assumed to be proportional to the square root of the effective confining pressure, which is a standard assumption in this program. For the sand and sandy silt (the 2nd, 3rd, 5th, 6th, 8th and 9th layers), ϕ_f was determined from the N values based on Morita et al. (1997). For the silt and clay (the 4th and 7th layers), a shear strength equivalent to $\phi_f=30°$ was used. For the porosity n and the maximum damping coefficient h_{max}, the values ordinarily used for FLIP analyses were used.

For the hatched layers in Table 3, the effects of excess pore pressure were considered. The parameters that control the excess pore pressure were determined from the N values and fine particle content based on Morita et al. (1997). The fine particle content was based on the laboratory test results for the 5th and 6th layers. For the 3rd, 8th and 9th layers, the author decided to use the same fine particle content as the 6th, 6th and 5th layers, respectively, considering the similarity of the soils and N values.

The input ground motions (NS and UD components in one case and EW and UD components in another case) were applied via a viscous boundary. In terms of the UD component, the result for the former case was
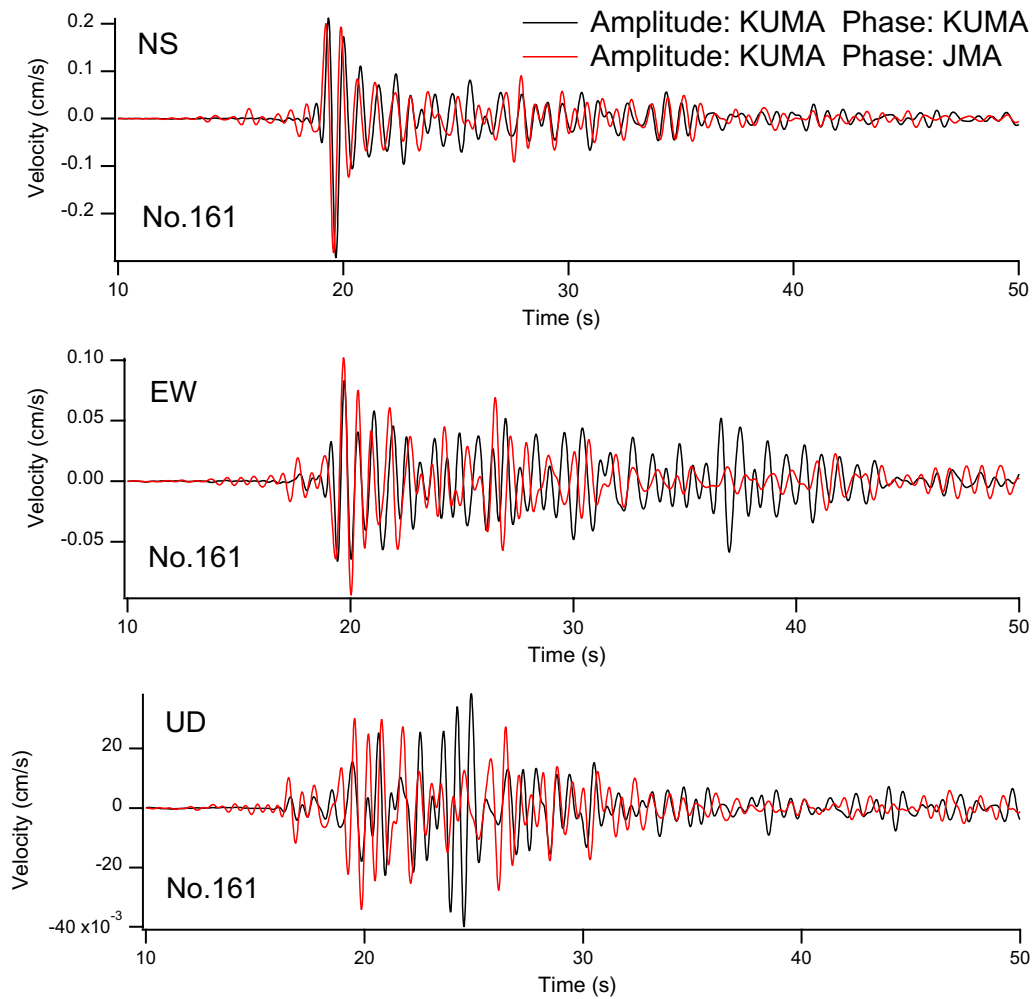
Fig. 11 Similarity of the Fourier phase characteristics between KUMA and JMA for the event No.161. The observed velocity waveforms for the event No.161 at KUMA (black traces) and the phase-exchanged velocity waveforms in which the Fourier amplitude at KUMA and the Fourier phase at JMA, both for the event No.161, are combined (red traces). Both traces are in the frequency range of 0.2–2 Hz

Table 2 Parameters used for the deconvolution analyses to estimate base outcrop motions

No.	Soil	Thickness (m)	VP (m/s)	VS (m/s)	Density (g/cm³)
1	Bank (gravel)	1.70	280.0	95.0	2.00
2*	Sandy silt	3.80	490.0	100.0	1.40
3	Sand with silt	2.20	1020.0	190.0	1.80
4*	Clay with sand	1.80	1160.0	120.0	1.30
5*	Sand	10.50	1550.0	190.0	1.90
6*	Sand with silt	3.70	3470.0	200.0	1.80
7*	Silt with sand	1.30	2160.0	230.0	1.50
8	Sand with silt	3.50	2160.0	210.0	1.80
9	Sand with gravel	2.50	1150.0	260.0	1.90
	Gravel	–	1440.0	290.0	2.00

For the layers marked by *, laboratory test results were available

Table 3 Parameters used for the effective stress analyses

Depth (m)	Thickness (m)	Soil	γ_t (kN/m³)	γ_t' (kN/m³)	N	σ_v' (kN/m²)	N65	Fc(%)	Vs(m/s)	σ_{m0}' (kN/m²)	G_{m0} (kN/m²)	K_{m0} (kN/m²)	ϕ (度)	mG、mK	n	hmax
−1.70	1.70	Gravel	19.6	19.6	—	16.7	—	—	95.0	—	—	—	—	—	—	—
−5.50	3.80	Sandy silt	13.4	13.4	2	58.8	2.4	—	100.0	44.1	13673	35658	39.00	0.500	0.450	0.240
−7.70	2.20	Sand with silt	17.6	7.8	22	92.8	19.3	21.9	190.0	69.6	64833	169073	42.00	0.500	0.450	0.240
−9.50	1.80	Clay with sand	12.6	2.8	—	103.9	—	—	120.0	77.9	18514	48282	30.00	0.500	0.550	0.203
−20.00	10.50	Sand	18.7	8.9	17	153.2	11.3	14.9	190.0	114.9	68885	179640	41.00	0.500	0.450	0.240
−23.70	3.70	Sand with silt	18.0	8.2	5	215.1	1.3	21.9	200.0	161.3	73469	191597	39.00	0.500	0.450	0.240
−25.00	1.30	Silt with sand	14.7	4.9	—	233.4	—	—	230.0	175.1	79350	206932	30.00	0.500	0.550	0.208
−28.50	3.50	Sand with silt	18.0	8.2	4	251.0	0.0	21.9	210.0	188.2	81000	211235	39.00	0.500	0.450	0.240
−31.00	2.50	Sand with gravel	18.7	8.9	24	276.4	10.7	14.9	260.0	207.3	128992	336390	42.00	0.500	0.450	0.240

γ_t: unit weight. γ_t': submerged unit weight. N: SPT N-value. σ_v': effective vertical stress. N_{65}: SPT N-value for a reference effective mean stress. F_c: fine particle content. V_S: shear wave velocity. σ_{m0}': reference effective confining pressure. G_{m0}: shear modulus for the soil skeleton at small strain for the reference effective confining pressure. K_{m0}: bulk modulus for the soil skeleton at small strain for the reference effective confining pressure. ϕ: internal friction angle. m_G: exponent that determines the dependence of the shear modulus for the soil skeleton at small strain on the effective confining pressure. m_K: exponent that determines the dependence of the bulk modulus for the soil skeleton at small strain on the effective confining pressure. n: porosity. h_{max}: maximum damping factor
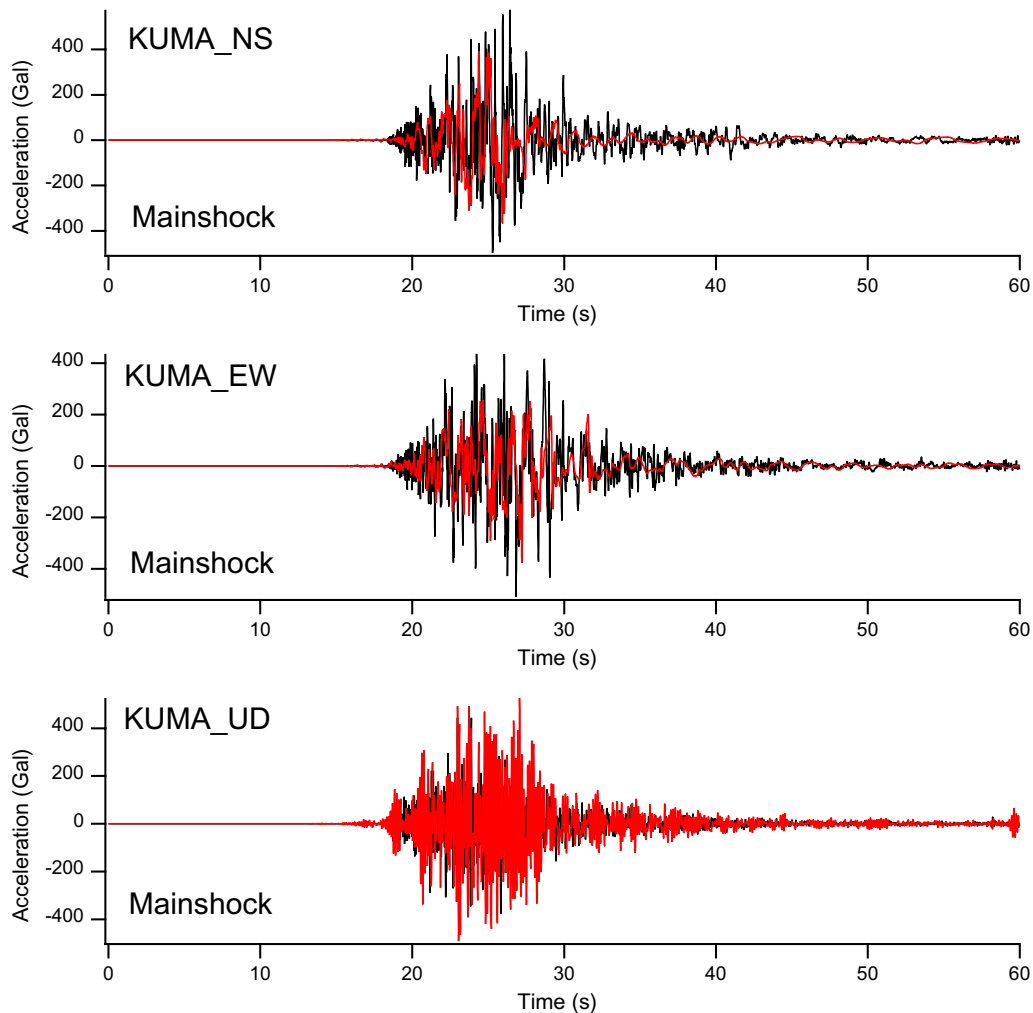

Fig. 12 Acceleration waveforms estimated for the blind prediction Step 3 for the mainshock. The acceleration waveforms estimated for the blind prediction Step 3 for the mainshock (red traces) are compared with the recorded acceleration waveforms distributed after the blind prediction (black traces). The origin of the horizontal axis corresponds to April 16, 2016, 1:24:50 (JST)

selected to be submitted. The difference of the UD components for the two cases was small.

Results

In Fig. 12, the acceleration waveforms estimated and submitted by the author for the blind prediction Step 3 for the mainshock are compared with the recorded acceleration waveforms, which were distributed by the organizer after the blind prediction. The main phases in the recorded waveforms are captured by the estimated waveforms. However, the amplitudes are underestimated especially for the NS component. In Fig. 13, the estimated velocity waveforms for the mainshock are compared with the velocity waveforms calculated from the records. The amplitudes are overestimated for the NS

component. In Fig. 14, the estimated Fourier spectra for the mainshock are compared with the Fourier spectra calculated from the records. For the NS component, the shift of the energy to lower frequency components in the estimated Fourier spectra due to soil nonlinearity is causing a discrepancy between the estimated and observed Fourier spectra. It could be pointed out that the simulation result for the EW component for the mainshock is good in terms of velocity waveforms and Fourier spectra. The S2 score (Anderson 2004) was 5.7, 7.5 and 6.5 for the NS, EW and UD broadband waveforms, respectively.

The results for the foreshock (Additional file 1: Figures A4–A6) [see appendix.pdf] showed a similar tendency. In the acceleration waveforms, the amplitudes were underestimated especially for the later phases. In
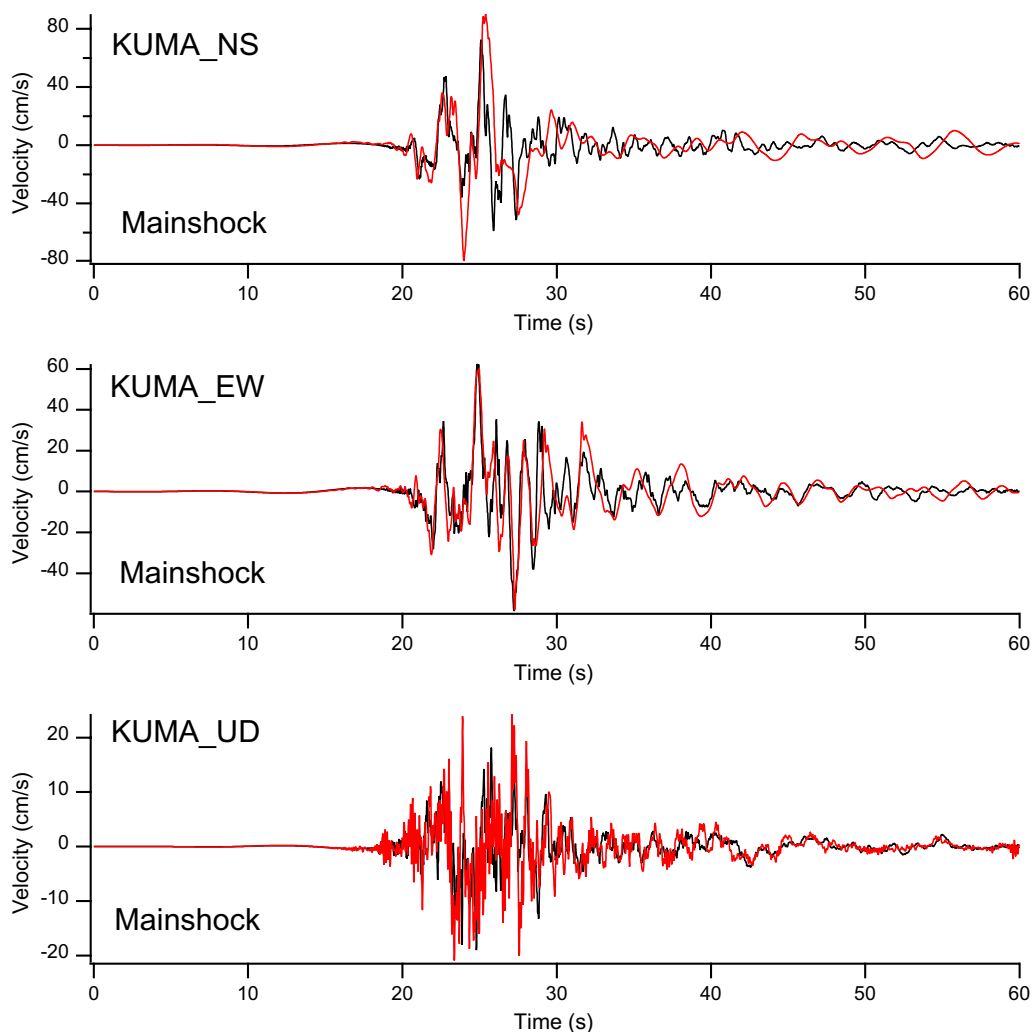

Fig. 13 Velocity waveforms estimated for the blind prediction Step 3 for the mainshock. The velocity waveforms estimated for the blind prediction Step 3 for the mainshock (red traces) are compared with the velocity waveforms calculated from the recorded acceleration waveforms distributed after the blind prediction (black traces). The origin of the horizontal axis corresponds to April 16, 2016, 1:24:50 (JST)
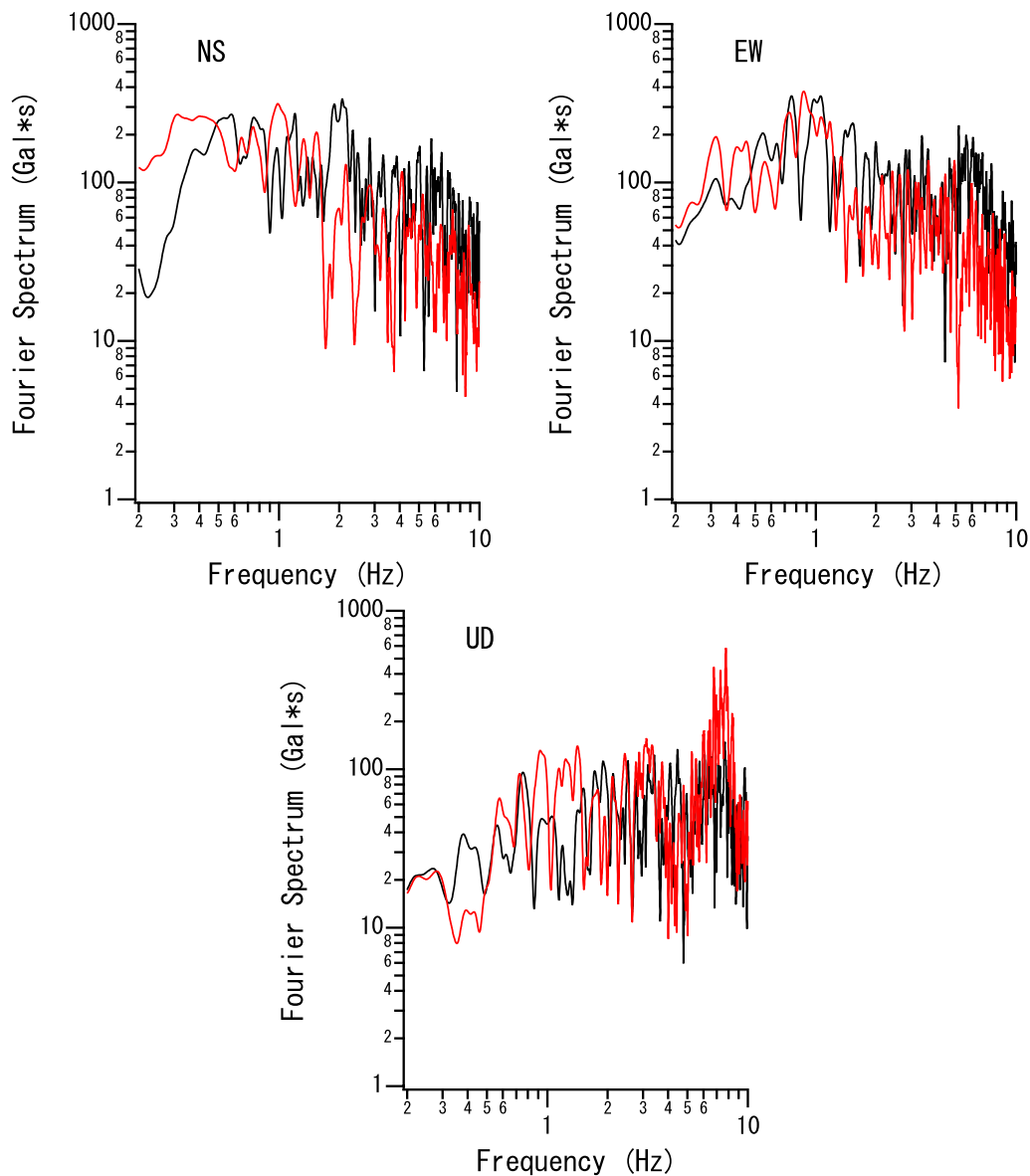
Fig. 14 Fourier spectra estimated for the blind prediction Step 3 for the mainshock. The Fourier spectra estimated for the blind prediction Step 3 for the mainshock (red traces) are compared with the Fourier spectra calculated from the recorded acceleration waveforms distributed after the blind prediction (black traces). The Fourier spectra are smoothed with a Parzen window of 0.05 Hz

the velocity waveforms, the amplitudes were overestimated. In the Fourier spectra, the shift of the energy to lower frequency components in the estimated Fourier spectra due to soil nonlinearity is causing a discrepancy between the estimated and observed Fourier spectra especially for the NS component. The S2 score (Anderson 2004) was 6.4, 7.5 and 5.0 for the NS, EW and UD broadband waveforms, respectively.

Discussion

The successful result for the blind prediction Step 2 indicated the effectiveness of the site-effect substitution method in estimating ground motions after an earthquake at a site where the ground motions are unknown as long as aftershock records are available at the site. One of the main features of the present method is that
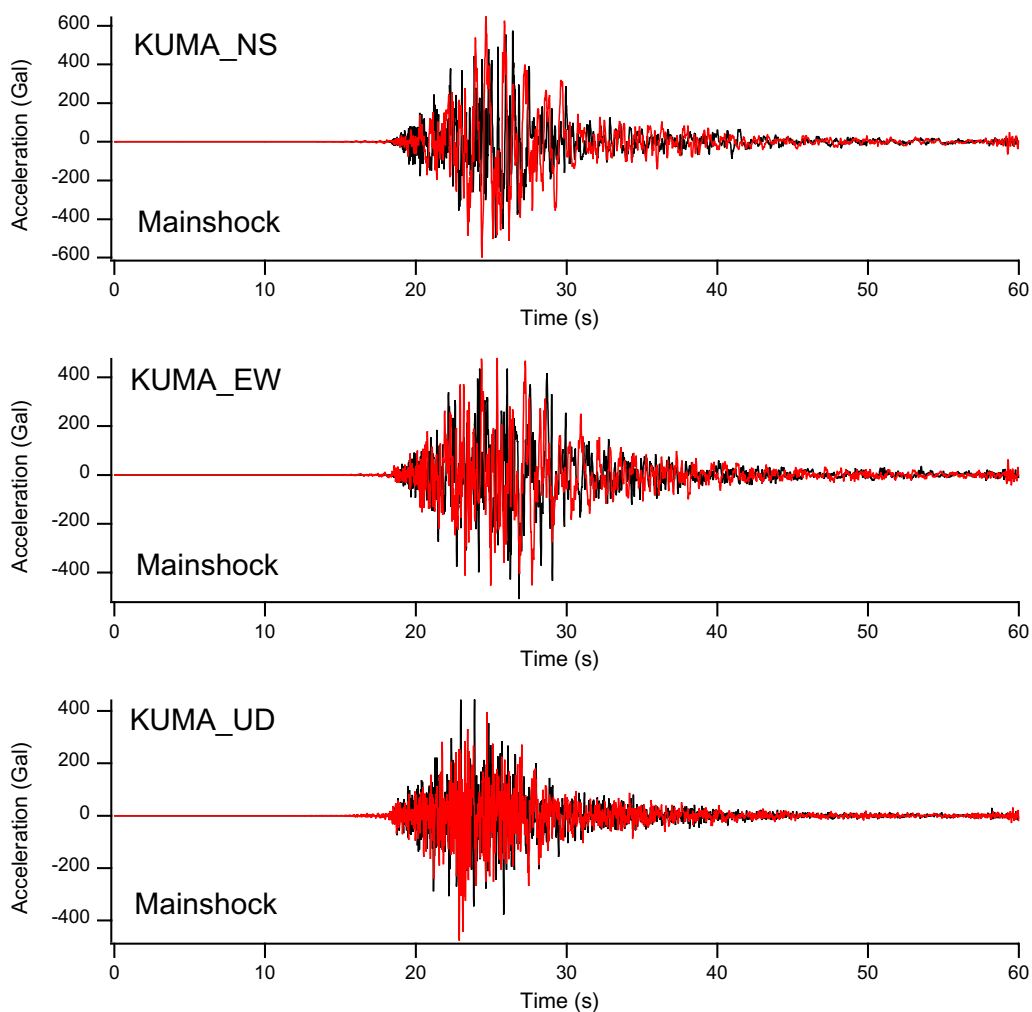
Fig. 15 Acceleration waveforms estimated for the mainshock under linear site response. The acceleration waveforms estimated for the mainshock under linear site response (red traces) are compared with the recorded acceleration waveforms (black traces). The origin of the horizontal axis corresponds to April 16, 2016, 1:24:50 (JST)

the Fourier phase characteristics of a single event is used rather than averaging Fourier phase spectra of different events. Averaging was avoided because it often affects the causality of generated time histories. The appropriateness of using the Fourier phase characteristics of a single event was shown by Hata et al. (2011) and also supported by the results of this study.

In the application of the site-effect substitution method, it is preferable to select an event that occurred near the target event to represent the Fourier phase characteristics appropriately. In Additional file 1: Figure A7 [see appendix.pdf], estimated NS-component velocity waveforms for the target event of the blind prediction Step 2 with different Fourier phase spectra are compared with the velocity waveforms calculated from the records. It can be seen that the estimated waveforms are dependent on the selection of the Fourier phase spectrum and

the event No.104, which is closest to the target event (Fig. 2) produced the best result.

It should be noted that two conditions contributed to the favorable result in Step 2. One is the fact that the rupture process of the target event was simple. As can be seen in Fig. 5, the Fourier phase spectra were interchangeable between the events No.35 and No.104. This means that the Fourier phase characteristics were almost determined by the path and site effects and not by the source effects. This is the evidence for a simple rupture process of the target event No.35. Another condition that contributed to the favorable result was that the soil nonlinearity at the target site was negligible. This was already discussed in terms of the bottom panel of Fig. 4 and supported by the accurate reproduction of the Fourier spectra in Fig. 9. These conditions were favorable for the application of the site-effect substitution method.
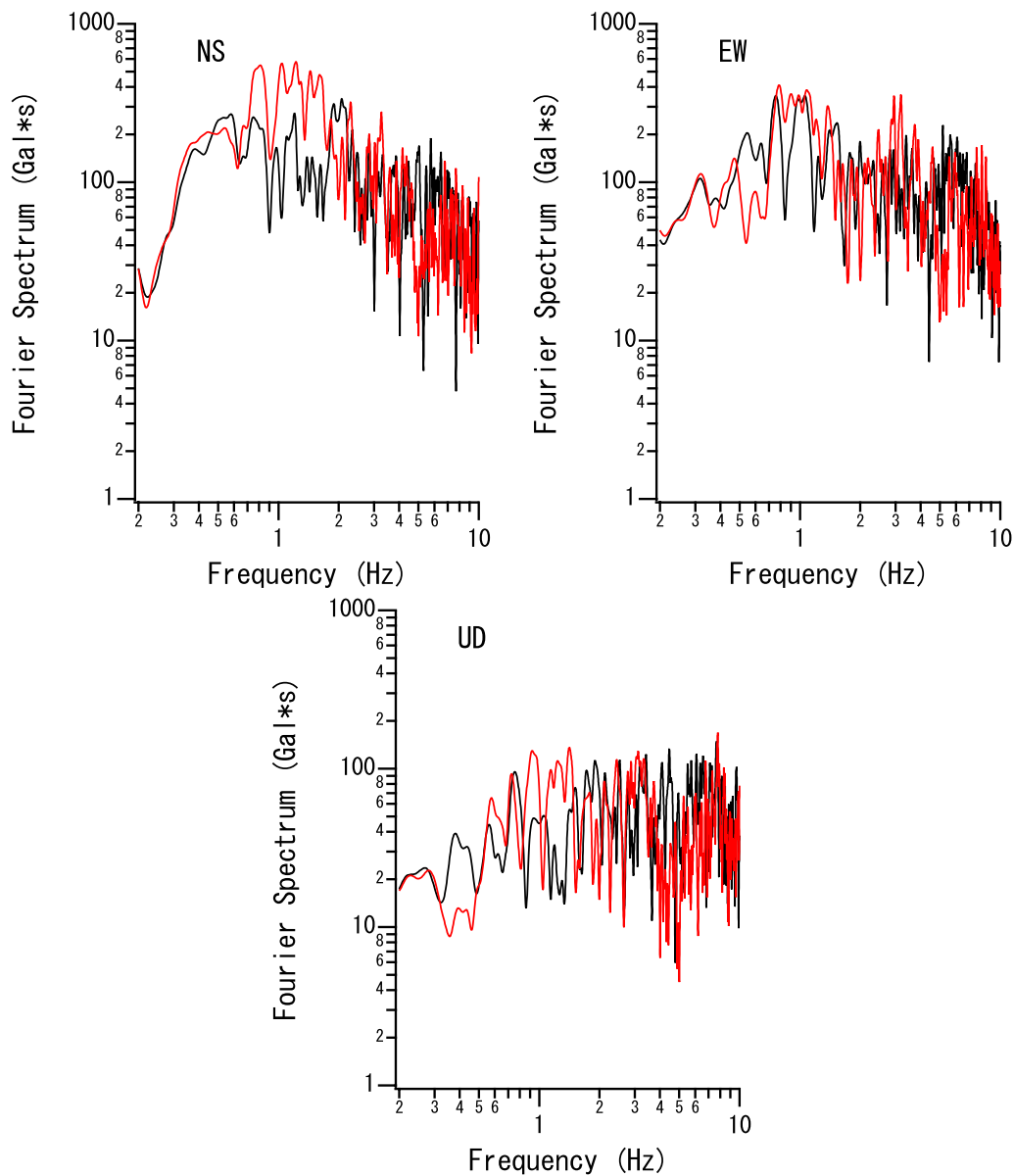
Fig. 16 Fourier spectra estimated for the mainshock under linear site response. The Fourier spectra estimated for the mainshock under linear site response (red traces) are compared with the Fourier spectra calculated from the recorded acceleration waveforms (black traces). The Fourier spectra are smoothed with a Parzen window of 0.05 Hz

The simulation results for the blind prediction Step 3 such as the underestimation of accelerations, overestimation of velocities and the shift of the energy to lower frequencies may be indicating that the strong soil nonlinearity considered in the effective stress analyses is the main cause of the discrepancy between the estimated and observed ground motions. Therefore, in the following, the estimated ground motions under the assumption of linear site response at KUMA, which were the intermediate product of the blind prediction, will be compared with the recorded ground motions.

In Fig. 15, the acceleration waveforms estimated for the mainshock under linear site response are compared with the recorded acceleration waveforms. In contrast to the results in Fig. 12, there was no underestimation in the amplitude of the acceleration waveforms. In Fig. 16, the Fourier spectra estimated for the mainshock under linear site response are compared with the Fourier spectra calculated from the records. In contrast to the results in Fig. 14, the shift of the energy to lower frequency components for the horizontal components was not evident and the estimated Fourier spectra were much closer to the

observed Fourier spectra. The results for the foreshock under linear site response (Additional file 1: Figures A8–A9) [see appendix.pdf] showed a similar tendency. In the acceleration waveforms (Additional file 1: Figure A8), there was no underestimation in the amplitude in contrast to the results shown in Additional file 1: Figure A4. In the Fourier spectra (Additional file 1: Figure A9), the shift of the energy to lower frequency components for the horizontal components was not evident and the estimated Fourier spectra were much closer to the observed Fourier spectra compared to Additional file 1: Figure A6. One explanation for this result could be that the nonlinear soil behavior at the target site KUMA during the foreshock and the mainshock of the 2016 Kumamoto earthquake sequence was not a strong one but rather a weak one that involved slight increase in the damping factor without a significant decrease in the soil stiffness. Another explanation for this result could be that the effect of soil nonlinearity was already included in the records at JMA, which was neglected in the procedure the author followed. Therefore, the effect of soil nonlinearity was double counted in the results submitted by the author.

Conclusions

In this article, the methods employed by the author and the results for the ESG6 Blind Prediction Steps 2&3 were described. The target event for Step 2 was the April 16, 2016, 3:03 (JST), M5.9 earthquake that occurred in the Aso region. To simulate ground motions at the target site KUMA during this earthquake, the author used the site-effect substitution method. The Fourier amplitude spectrum was estimated from the spectral ratio between KUMA and a nearby station JMA. The Fourier phase spectrum was approximated by the spectrum at KUMA for another event that occurred in the Aso region. Comparison between the estimated and recorded ground motions after the blind prediction revealed that, except for the error in the arrival time, the estimated ground motions were fairly consistent with the observed ground motions. The result indicates the effectiveness of the site-effect substitution method when the rupture process of the target event is simple and the soil nonlinearity at the target site is not significant. The target events for Step 3 were the M6.5 foreshock and the M7.3 mainshock of the 2016 Kumamoto earthquake sequence. To simulate ground motions at KUMA during these earthquakes, the author used a similar method to estimate the Fourier amplitude spectrum, however, the author simply used the Fourier phase spectrum at JMA for the target events. Then, the author conducted effective stress analyses using a program called "FLIP". The parameters were determined based on a simplified procedure from the PS logging results, N values and fine particle content. Comparison between the estimated and recorded ground motions after the blind prediction indicated that, although the estimated ground motions captured the main phases of the recorded ground motions, the low-frequency components were overestimated and the high-frequency components were underestimated in the horizontal components. The strong soil nonlinearity considered in the effective stress analyses was the main cause of the discrepancy between the estimated and observed ground motions. One explanation for this result could be that the nonlinear soil behavior at KUMA during the foreshock and the mainshock was not a strong one without a significant decrease in the soil stiffness. Another explanation could be that the effect of soil nonlinearity was already included in the records at JMA and the effect of soil nonlinearity was double counted in the results submitted by the author.

Abbreviation
JMA   Japan Meteorological Agency

Supplementary Information

The online version contains supplementary material available at https://doi.org/10.1186/s40623-023-01854-z.

> **Additional file 1:** Appendix Figures A1–A9.

Availability of data and materials
The strong motion data at the station abbreviated as "JMA" in this article can be purchased from the Japan Meteorological Business Support Center.

Declarations

Ethics approval and consent to participate
Not applicable.

Consent for publication
Not applicable.

Competing interests
Not applicable.

Author details
[1]Director of Earthquake Disaster Prevention Engineering Department, Port and Airport Research Institute, 3-1-1, Nagase, Yokosuka 239-0826, Japan.

References

Aki K (1993) Local site effects on weak and strong ground motion. Tectonophysics 218:93–111

Anderson JG (2004) Quantitative measure of the goodness-of-fit of synthetic seismograms. Proceedings of the 13th World Conference on Earthquake Engineering, Paper No. 243

Asano K, Iwata T (2016) Source rupture processes of the foreshock and mainshock in the 2016 Kumamoto earthquake sequence estimated from the kinematic waveform inversion of strong motion data. Earth Planets Space 68:147. https://doi.org/10.1186/s40623-016-0519-9

Beauval C, Bard PY, Moczo P, Kristek J (2003) Quantification of frequency-dependent lengthening of seismic ground motion duration due to local geology: application to the Volvi Area (Greece). Bull Seismol Soc Am 93:371–385

Beresnev IA, Wen KL (1996) Nonlinear soil response: a reality? Bull Seismol Soc Am 86:1964–1978

Boore DM (2003) Phase derivatives and simulation of strong ground motions. Bull Seismol Soc Am 93:1132–1143

Chimoto K, Yamanaka H, Tsuno S, Matsushima S (2022) Predicted results of the velocity structure at the target site of the blind prediction exercise from microtremors and surface wave method as step-1, -report of the experiments for "the 6th international symposium on effects of surface geology on seismic motion." Earth Planets Space. https://doi.org/10.1186/s40623-023-01842-3

Danmura H, Miyata M, Nozu A, Wakai A, Asai S (2013) A study on the simple estimation method for residual deformation of quay walls considering the effect of ground liquefaction during earthquake. Technical Note of NILIM 743 (in Japanese with English abstract)

Hata Y, Nozu A, Ichii K (2011) A practical method to estimate strong ground motions after an earthquake, based on site amplification and phase characteristics. Bull Seismol Soc Am 101:688–700

Hutchings L, Jarpe S (1996) Ground-motion variability at the Highway 14 and I-5 interchange in the northern San Fernando Valley. Bull Seismol Soc Am 86:289–299

Iai S, Matsunaga Y, Kameoka T (1992) Strain space plasticity model for cyclic mobility. Soils Found 32:1–15

Iai S, Morita T, Kameoka T, Matsunaga Y, Abiko K (1995) Response of a dense sand deposit during 1993 Kushiro-oki earthquake. Soils Found 35:115–131

Iai S, Ichii K, Liu H, Morita T (1998) Effective stress analyses of port structures. Spec Issue Soils Found 38:97–114

Iai S (1991) A strain space multiple mechanism model for cyclic behavior of sand and its application. Earthquake Engineering Research Note 43. https://www.pari.go.jp/bsh/jbn-kzo/jbn-bsi/taisin/related/rela002.pdf. Accessed 27 Sep 2022

International Organization for Standardization (2005) ISO23469: Bases for design of structures—Seismic actions for designing geotechnical works

Kamae K, Irikura K (1998) Source model of the 1995 Hyogo-ken Nanbu earthquake and simulation of near-source ground motion. Bull Seismol Soc Am 88:400–412

Kanai K (1952) Relation between the nature of surface layer and the amplitudes of earthquake motions. Bull Earthq Res Inst Univ Tokyo 30:31–37

Lysmer J, Kuhlemeyer RL (1969) Finite dynamic model for infinite media. J Eng Mech Div 95:859–877

Lysmer J, Seed HB, Schnabel PB (1971) Influence of base-rock characteristics on ground response. Bull Seismol Soc Am 61:1213–1231

Matsushima S, Yamanaka H, Tsuno S, Chimoto K, Suzuki H, Kawase H (2022) Investigation of the subsurface structure at the target site in Kumamoto, Japan and the distributed data of the blind prediction exercise, -Report of the experiments for "The 6th International Symposium on Effects of Surface Geology on Seismic Motion". Earth Planets and Space, submitted

Morita T, Iai S, Liu H, Ichii K, Sato Y (1997) Simplified method to determine parameter of FLIP. Technical Note of the Port and Harbour Research Institute 869. https://www.pari.go.jp/search-pdf/no0869.pdf. Accessed 27 Sep 2022 (in Japanese with English abstract)

Nozu A (2017) Differentiability of phase spectrum of earthquake ground motion and improvement of numerical calculation of group delay time. J Jpn Soc Civil Eng Ser A1(73):187

Nozu A (2022) Differentiability of phase spectrum of earthquake ground motion and improvement of numerical calculation of group delay time: a supplementary work. J Jpn Soc Civil Eng. https://doi.org/10.2208/jscejseee.78.4_I_737

Nozu A, Nagasaka Y (2017) Rupture process of the main shock of the 2016 Kumamoto earthquake with special reference to damaging ground motions: waveform inversion with empirical Green's functions. Earth Planets Space 69:22. https://doi.org/10.1186/s40623-017-0609-3

Nozu A, Nagao T, Yamada M (2009) Simulation of strong ground motions using empirical site amplification and phase characteristics: modification to incorporate causality. J Jpn Soc Civil Eng A 65:808–813

Sato T, Murono Y, Nishimura A (2000) Empirical modeling of phase spectrum of earthquake motion. Journal of Japan Society of Civil Engineers 640/I-50: 119–130 (in Japanese with English abstract)

Satoh T, Uetake T, Sugawara Y (1997) A study on empirical envelope model of long period strong motions by using group delay time. J Struct Constr Eng Archit Inst Jpn 493:31–39

Sawada S, Morikawa H, Toki K, Yokoyama K (1998) Identification of path and local site effects on phase spectrum of seismic motion. In: Proceedings of the 10th Japan Earthquake Engineering Symposium, Yokohama, Japan, 25–27 November 1998 (in Japanese with English abstract)

Schnabel PB, Lysmer J, Seed HB (1972) SHAKE—A computer program for earthquake response analysis of horizontally layered sites. Report No. EERC 72–12, Col. of Eng., University of California at Berkeley.

Tobita T, Iai S, Iwata T (2010) Numerical analysis of near-field asymmetric vertical motion. Bull Seismol Soc Am 100:1456–1469

Tsuno S, Nagashima F, Kawase H, Yamanaka H, Matsushima S (2022) Predicted results of the weak and strong ground motions at the target site of the blind prediction exercise as Step-2 and Step-3, -Report of the experiments for "The 6th International Symposium on Effects of Surface Geology on Seismic Motion". Earth Planets and Space, submitted

Yamanaka H, Chimoto K, Miyake H, Tsuno S, Yamada N (2016) Observation of earthquake ground motion due to aftershocks of the 2016 Kumamoto earthquake in damaged areas. Earth Planets Space 68:197. https://doi.org/10.1186/s40623-016-0574-2

Publisher's Note